Computing the melting point and thermodynamic stability of the orthorhombic and monoclinic crystalline polymorphs of the ionic liquid 1-n-butyl-3-methylimidazolium chloride

2 AUTHORS:

Sai Jayaraman
Massachusetts Institute of Technology
12 PUBLICATIONS **108** CITATIONS

SEE PROFILE

Edward J Maginn
University of Notre Dame
204 PUBLICATIONS **9,468** CITATIONS

SEE PROFILE

Computing the melting point and thermodynamic stability of the orthorhombic and monoclinic crystalline polymorphs of the ionic liquid 1-*n*-butyl-3-methylimidazolium chloride

Saivenkataraman Jayaraman and Edward J. Maginn[a)]
Department of Chemical and Biomolecular Engineering, University of Notre Dame, Notre Dame, Indiana 46556, USA

The melting point, enthalpy of fusion, and thermodynamic stability of two crystal polymorphs of the ionic liquid 1-*n*-butyl-3-methylimidazolium chloride are calculated using a thermodynamic integration-based atomistic simulation method. The computed melting point of the orthorhombic phase ranges from 365 to 369 K, depending on the classical force field used. This compares reasonably well with the experimental values, which range from 337 to 339 K. The computed enthalpy of fusion ranges from 19 to 29 kJ/mol, compared to the experimental values of 18.5 −21.5 kJ/mol. Only one of the two force fields evaluated in this work yielded a stable monoclinic phase, despite the fact that both give accurate liquid state densities. The computed melting point of the monoclinic polymorph was found to be 373 K, which is somewhat higher than the experimental range of 318–340 K. The computed enthalpy of fusion was 23 kJ/mol, which is also higher than the experimental value of 9.3−14.5 kJ/mol. The simulations predict that the monoclinic form is more stable than the orthorhombic form at low temperature, in agreement with one set of experiments but in conflict with another. The difference in free energy between the two polymorphs is very small, due to the fact that a single trans-gauche conformational difference in an alkyl sidechain distinguishes the two structures. As a result, it is very difficult to construct simple classical force fields that are accurate enough to definitively predict which polymorph is most stable. A liquid phase analysis of the probability distribution of the dihedral angles in the alkyl chain indicates that less than half of the dihedral angles are in the gauche-trans configuration that is adopted in the orthorhombic crystal. The low melting point and glass forming tendency of this ionic liquid is likely due to the energy barrier for conversion of the remaining dihedral angles into the gauche-trans state. The simulation procedure used to perform the melting point calculations is an extension of the so-called pseudosupercritical path sampling procedure. This study demonstrates that the method can be effectively applied to quite complex systems such as ionic liquids and that the appropriate choice of tethering potentials for a key step in the thermodynamic path can enable first order phase transitions to be avoided. © *2007 American Institute of Physics.* [DOI: 10.1063/1.2801539]

I. INTRODUCTION

Most inorganic molten salts have extremely high melting points, which limits their practical use. By careful choice of cation and anion, however, it is possible to prepare salts that have melting points that are below 100 °C; in some cases, melting points significantly lower than ambient temperatures are possible. These materials have been dubbed "ionic liquids" and have attracted a great deal of interest in recent years.[1] Ionic liquids can be made which have extremely low volatility, high thermal stability, and favorable solvation properties. This makes them interesting for a number of potential applications, including use as solvents, electrolytes, separation agents, and lubricants. Interestingly, low melting salts have been known for some time. One of the earliest reported ionic liquids is ethylammonium nitrate, which has a melting point of 12 °C.[2,3] Only in the last 15 years or so, however, has the potential of this class of material caught the attention of industry and the research community.[4]

Given that an ionic liquid is differentiated from a conventional molten salt by its melting point, it is apparent that understanding the link between chemical structure and melting point of ionic liquids is crucial. Generally speaking, it is desirable to have as low a melting point as possible, which maximizes the range over which the material may be used as a liquid. For some applications, however, it may be preferable to have melting points at intermediate temperatures. There are no completely reliable methods available for predicting how melting points will depend on the chemical structure or composition of an ionic liquid, which is unfortunate because it is known that small changes in the structure of an ionic liquid can have dramatic effects on the melting point. For alkylimidazolium cations, it has been observed that melting points drop rapidly as the alkyl chain attached to the 1-position on the ring increases in length from one up to about six to eight carbons. As the alkyl chain length increases further, melting temperatures increase, although the actual trend depends on the nature of the associated anion.[5] It has also been observed that the more asymmetric the cation

a)Electronic mail: ed@nd.edu

and the larger the anion, the lower the melting point tends to be. These heuristics are not always reliable, however, and so often efforts to synthesize new ionic liquids are frustrated by the fact that the target compound may turn out unexpectedly to be a high-melting solid.

There have been a number of computational efforts aimed at making a quantitative link between melting point and structure. Chief among these are the quantitative structure-property relationship (QSPR) modeling efforts. In QSPR, a limited amount of experimental data is used to develop correlations for a property (in this case, melting point) using molecular-based descriptors. This correlation can then be used to make limited predictions of melting points for molecules not too dissimilar from those used in developing the correlation. QSPR has been used to correlate/predict melting points for pyridinium and imidazolium-based salts[6–9] as well as quaternary ammonium[8] and triazolium salts.[10] These approaches do a reasonable job correlating melting points and making limited predictions, but the nature of the descriptors used in the correlations often limits the amount of physical insight one obtains into why a particular compound has a high or low melting point. The biggest drawback, however, is that a fairly large amount of experimental data is required before a correlation can be developed.

Atomistic-level simulations[11] are another powerful computational tool that can be used to gain physical insight into how the composition and structure of an ionic liquid is related to its properties. Unlike QSPR, these simulations are predictive in that little or no experimental data are required to develop the parameters that go into the models. Using classical potential functions derived from a mix of *ab initio* calculations and previous liquid-state simulations, several groups[12–18] have shown that liquid phase properties of ionic liquids can be accurately modeled. Far fewer studies have been carried out on the solid phase[19–21] and, to our knowledge, only Thompson and Alavi[20,22] have used atomistic simulations to compute the melting point of an ionic liquid. Melting point calculations are extremely demanding even for simple systems, and the added complexity involved with ionic liquids makes these systems a real challenge for modeling, which is one reason there have been few studies to date.

Alavi and Thompson[20,22] used a method pioneered by their group called "void-induced melting" to compute the melting point of an ionic liquid. In this method, which mimics an actual melting experiment, constant pressure molecular dynamics (MD) simulations are run on the crystal phase at increasing temperature until evidence of a first order melting transition is observed. Typically, an abrupt change in density is a signature of a melting transition. Due to the short time scales accessible by MD and the free energy barrier required to observe homogeneous nucleation in a perfect crystal, however, the melting transitions (or, more properly, point of thermal instability[23]) occurs at higher temperatures than the true melting point. In some cases, several hundred degrees of superheat are required for melting to occur.[20] To overcome this, the void induced melting method systematically creates voids in the crystal by gradually removing atoms or ion pairs from the lattice. As the void density in-

creases, the apparent melting point obtained from the constant pressure simulations decreases. At a void density of between 6% and 10%, it is observed that the apparent melting point levels off and this value is taken as the true melting point. At void densities above 10%, the crystal becomes mechanically unstable. This approach has been applied by the Thompson group to a wide range of materials.[24–26]

Besides void-induced melting, a number of other techniques can be used to compute the melting point of crystals. These can be placed into one of two categories: direct methods and free energy methods. Direct methods generally involve the formation of an interface between crystalline and liquid phases, with the melting point determined from the temperature and pressure that yields a stable interface.[27–30] This method works because the free energy barrier for heterogeneous nucleation is much lower than that for homogeneous nucleation. While interfacial methods are successful and relatively straightforward to apply, some questions remain about whether finite-size effects are properly accounted for,[31] and different crystal surfaces may have different apparent melting points. In addition, most interfacial simulations have been carried out on systems with little to no intramolecular degrees of freedom. For molecular crystals where cooperative orientational degrees of freedom are both slow and important, interfacial MD simulations may not be capable of adequately probing heterogeneous nucleation on MD time scales. This issue needs to be probed further in future work.

The second type of melting point simulation approach is based on satisfying the phase equilibrium condition, namely equality of temperature, pressure, and Gibbs energy. Within this broad category, there are a number of particular techniques, including thermodynamic integration[32] and phase switch[33] approaches. While these methods provide a rigorous way of calculating melting points, they are generally more difficult to implement than either interfacial methods or void induced melting, and no system as complicated as an ionic liquid has been examined with these techniques. Recently, we have extended a thermodynamic integration procedure[34,35] originally proposed by Grochola[36,37] and applied it to molten sodium chloride and the Lennard–Jones fluid.[34] Subsequently, we extended the method to handle multiatom molecules such as benzene and triazole.[35] The method, alternatively referred to as constrained fluid λ integration or pseudosupercritical path sampling, overcomes some of the limitations of traditional thermodynamic integration methods because it does not require fluid and solid reference state absolute free energies. In the present work, we apply the method to compute the melting point and free energy differences of two stable polymorphs of 1-*n*-butyl-3-methylimidazolium chloride ([C$_4$mim][Cl]), a complex ionic liquid containing many flexible intramolecular degrees of freedom.

[C$_4$mim][Cl] is an ideal system to study with atomistic simulation. The most widely investigated ionic liquids to date contain imidazolium cations and the [C$_4$mim] cation is perhaps the most widely studied within this category. The melting point and crystal structure of two polymorphs of [C$_4$mim][Cl] (orthorhombic and monoclinic) have been independently measured by two groups.[38–41] Interestingly, al-
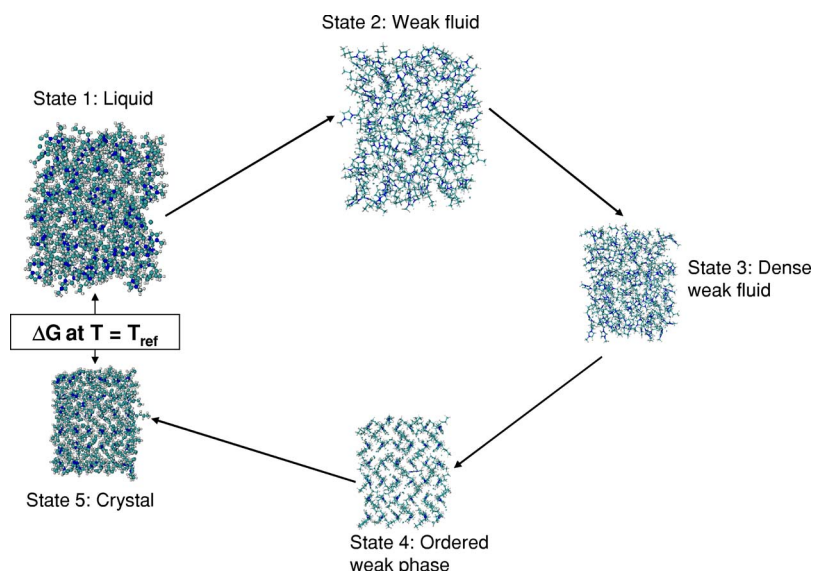
FIG. 1. (Color online) A schematic of the thermodynamic cycle used in this method.

though there is experimental agreement on the crystal structures, there are conflicting reports as to which polymorph is the most thermodynamically stable. Holbrey and co-workers reported that the orthorhombic phase is most stable,[38] with a melting point of 66 °C. They observed that the monoclinic form displayed a transition at 41 °C characteristic of a plastic crystal transition. Hamaguchi *et al.* reported the melting point of the orthorhombic phase as 64 °C,[42] in good agreement with the value given by Holbrey *et al.* For the monoclinic phase, they reported that the melting point ranged from 47 to 67 °C, depending on the particular crystal. Interestingly, they observed that the orthorhombic phase intercoverted to the monoclinic phase when held at dry ice temperatures for 24 h,[42] suggesting that the orthorhombic phase is metastable and that the monoclinic phase is actually the thermodynamically stable form of the crystal at low temperature. Both groups agree that a subtle trans-gauche conformational difference in the butyl chain is responsible for the differences in crystal structures. Moreover, liquid phase Raman studies have suggested that both alkyl chain conformations are present in the liquid state.[40]

II. METHODOLOGY

A. Simulation procedure

To compute the melting point and free energy differences of the two polymorphs of $[C_4mim][Cl]$ at a pressure of 1 atm, the temperature at which the liquid and crystalline states have equal free energies was computed using the pseudo-upercritical path sampling method. Extensive details of the method are provided elsewhere,[34,35] so only those details specific to this particular system are provided here. We also take this opportunity (see later) to correct two typographical errors that appeared in our previous work.[35]

The calculation procedure involves two parts. First, relative free energy curves are computed for the liquid and crystalline phases by carrying out a series of isothermal-isobaric (NPT) MD simulations. The enthalpy of each phase is computed as a function of temperature, and the Gibbs–Helmholtz equation is integrated to obtain Gibbs free energies relative to an arbitrary reference temperature T_{ref},

$$\frac{G}{RT} - \left(\frac{G}{RT}\right)_{ref} = \int_{T_{ref}}^{T} -\frac{H}{RT^2} dT. \tag{1}$$

The second part of the calculation involves the use of thermodynamic integration to compute the free energy difference along a thermodynamic path between the liquid and crystalline phases at the reference temperature. Note that once this difference is known for each polymorph, the free energy difference between the two crystal polymorphs is also known. Essentially, this step gives the constant of integration $(G/RT)_{ref}$ in Eq. (1). From this, the temperature at which the liquid and crystalline free energies are equal can be found, which is the melting temperature. This procedure differs from commonly used reference state approaches,[32] where the absolute free energy of the liquid and crystal is obtained by integrating along two separate paths to reference states of known free energy.

There are five separate states along the thermodynamic path, all at the reference temperature: (1) the liquid at a density corresponding to the pressure of interest; (2) a weakly interacting fluid at the liquid density; (3) a weakly interacting fluid at the crystalline phase density; (4) an ordered weakly interacting state at the crystal density; and (5) the crystal at the pressure of interest. This is illustrated in Fig. 1.

Specific transitions between all adjacent states i and j (except $2 \rightarrow 3$) are accomplished by changes in a coupling parameter λ, with the Helmholtz free energy change between states computed by

$$\Delta A_{i \rightarrow j} = \int_0^1 \left\langle \frac{\partial U}{\partial \lambda} \right\rangle_\lambda d\lambda, \tag{2}$$

where U is the potential energy of the system and the pointed brackets indicate an ensemble average. The coupling parameter λ is defined such that at $\lambda = 0$ state (i) is recovered and at $\lambda = 1$ state (j) is recovered. The free energy change associ-

ated with moving from states (2) to (3) is given by the thermodynamic identity

$$\Delta A_{2\to3} = \int_{V^\ell}^{V^S} -\langle P\rangle dV, \tag{3}$$

where V^ℓ and V^S are the molar volumes of the liquid and solid phases, respectively.

State (4) is ordered by turning on an external potential that tethers the ion centers of mass and selected atoms to lattice sites corresponding to the structure of state (5). There is a great deal of flexibility as to how the tethering potential is chosen. As shown later, the strength of the tethering potentials affect the numerical accuracy and efficiency of the integration between states (3) and (4). This issue will be addressed in detail later. Consistent with our previous work,[35] we have used three-dimensional harmonic oscillators to order the fluid, where the probability distribution of an atom or center of mass of an ion about its average position is given by

$$P(r) = \left(\frac{\beta\kappa}{\pi}\right)^{3/2} 4\pi r^2 \exp(-\beta\kappa r^2) dr. \tag{4}$$

Note that the factor dr was missing in our previous work.[35] The total potential energy function used in moving between states (3) and (4) is given by

$$U_{3\to4}(\lambda) = \eta^m U^{\text{VDW}} + \eta^n U^{\text{ELEC}} + U^{\text{NS}}$$
$$- \lambda\sum_i\sum_j a_{ij}\exp(-b_{ij}r_{ij}^2), \tag{5}$$

where U^{VDW} and U^{ELEC} are the unscaled van der Waals and Coulombic intermolecular energies. U^{NS} is all the nonscaled potential energy terms, which in this case consists of all intramolecular potential terms. Parameters m, n, and η were chosen as 1, 2, and 0.1, respectively. The well depth and width are controlled by the parameters a_{ij} and b_{ij}.[35]

In moving between states (4) and (5), the tethering potential is turned off and full intermolecular interactions are restored. The potential energy expression for this step is

$$U_{4\to5}(\lambda) = [\eta+\lambda(1-\eta)]^m U^{\text{VDW}} + [\eta+\lambda(1-\eta)]^n U^{\text{ELEC}}$$
$$+ U^{\text{NS}} - (1-\lambda)\sum_i\sum_j a_{ij}\exp(-b_{ij}r_{ij}^2). \tag{6}$$

Note that this differs slightly from Eq. (7) in Ref. 35, which contained a typographical error.

B. Simulation details

Two different force fields were tested for the ionic liquid. The first force field was taken from the work of Canongia Lopes and Pádua[19] and is designated as CLP. Updated parameters for the CLP potential were obtained from the internet as of February 2007.[43] A second force field consisting of cation parameters from Cadena and Maginn[21] and chloride parameters from Jensen and Jorgensen[44] was also considered for this study. This force field will be designated as CMJJ. The CLP potential is based on the OPLS force field, with some of the torsional interactions of the imidazolium ring and alkyl side chains determined from *ab initio*

calculations on the gas phase cation. The cation torsion parameters in the CMJJ potential are from the CHARMM force field.

The CLP force field is a partially flexible model in which the C-H bonds of the cation are held rigid. The CMJJ force field is fully flexible. For the NPT simulations of the CLP model, the integrator developed by Melchionna et al.[45] was used to simplify the implementation of constraints. A time step of 1 fs was used for the NPT simulations conducted using the CLP force field. The NPT simulations with the CMJJ model used a standard Nosé–Hoover algorithm[46] with a 1 fs time step for all forces. Cutoffs of 11 Å were used for both Lennard–Jones and the real-space electrostatic interactions. The smooth particle mesh Ewald method[47] was used for handling long-range electrostatic interactions with a damping parameter of 0.2992 Å and 32 mesh points in all directions. All simulations were carried out using locally developed software. This code has been validated against the widely used molecular dynamics packages DL_POLY[48] and NAMD.[49]

To obtain the relative free energy curves for the crystal and liquid via Eq. (1), NPT MD simulations were conducted on 108 ion pairs for the orthorhombic calculations and 144 ion pairs for the monoclinic calculations at 1 atm pressure and temperatures varying from 300 to 400 K. The crystal phase simulations were carried out on a $3\times3\times3$ supercell for the orthorhombic phase and on a $3\times3\times4$ supercell for the monoclinic phase. A larger system was used for the monoclinic simulations so as to accommodate the choice of Lennard–Jones cutoff distance. For the liquid phase simulations, volume fluctuations were isotropic, while for the crystalline phase an anisotropic flexible cell algorithm[50] was used. The starting configurations for the orthorhombic and monoclinic phases were taken from the experimental unit cell obtained from x-ray diffraction measurements.[38] Once relative free energy curves were generated, thermodynamic cycle calculations were carried out in the canonical (NVT) ensemble at a reference temperature of 380 K.

It is important when computing quantities such as melting points to be able to quantify the error. The uncertainty in the quantity $\langle\partial U/\partial\lambda\rangle$ in Eq. (2) or average pressure in Eq. (3) for each point on the thermodynamic integration cycle was estimated as the standard deviation of the mean obtained using a 20-block average. For any quantity A, the average of each block i was calculated as

$$A_i' = \frac{1}{N/20}\sum_{j=20(i-1)+1}^{20i} A_j, \tag{7}$$

where N is the total number of observations of A available. The ensemble average or mean of A is given by

$$\langle A\rangle \approx \bar{A}' = \frac{1}{20}\sum_{i=1}^{20} A_i', \tag{8}$$

where $\bar{A}'$ is the average of the 20-block sample. The uncertainty is taken as the standard deviation of the mean, which is given by

TABLE I. Comparison of experimental and simulation cell parameters at 173 K and 1 atm for the orthorhombic phase of [C$_4$mim][Cl]. Cell lengths a, b, and c are in angstroms (Å) and cell angles α, β, and γ are in degrees. Subscripted values depict statistical uncertainty in the final digit.

	a	b	c	α	β	γ
Experimental[a]	10.113	11.411	8.3285	90.0	90.0	90.0
Simulation[b]	9.745$_8$	11.730$_9$	8.504$_3$	90.00$_6$	90.00$_8$	90.00$_4$
Simulation[c]	10.10$_1$	11.55$_1$	8.681$_8$	90.11$_7$	89.90$_8$	90.00$_5$

[a]Values obtained from Ref. 38.
[b]Values obtained from present study using CLP force field.
[c]Values obtained from present study using CMJJ force field.

$$\sigma(A) = \sqrt{\frac{\sigma^2(A')}{19}}, \tag{9}$$

where the variance of the sample is

$$\sigma^2(A') = \frac{1}{20}\sum_{i=1}^{20} A_i'^2 - \bar{A}'^2. \tag{10}$$

To carry out the integrations given by Eqs. (2) and (3) for each step along the thermodynamic cycle, the free energy curves must be smooth and integrable. Hermite polynomials were used to interpolate between discrete $\langle \partial U/\partial\lambda \rangle_\lambda$ and $\langle P \rangle$ values and then the integrations were carried out using the MATLAB (version 7.3.0.298) package. The uncertainty of each of the discrete points was used to estimate the uncertainty of the integrals in Eqs. (2) and (3) in the following manner. It was assumed that the discrete points $\langle \partial U/\partial\lambda \rangle_\lambda$ and $\langle P \rangle$ were normally distributed about their mean, with variance given by Eq. (10). A Monte Carlo sampling procedure was then used to randomly generate 1000 representative points at each λ from this normal distribution. Hermite polynomials were fit to the 1000 sets of data points generated in this manner and then each fit was integrated and taken as an independent estimate of the free energy change. The estimated free energy change of a particular transformation was taken as the average of these individual free energy changes and the uncertainty was estimated as the standard deviation. The total uncertainty in the free energy difference was obtained by propagating the uncertainties of each transformation step. Finally, this total uncertainty was used to estimate the uncertainty of the computed melting point.

III. RESULTS

A. Crystal phase simulations

Before beginning the melting point calculations, NPT MD simulations were carried out on both crystal polymorphs at 300 K and 1 atm using the CLP and CMJJ potential models. Surprisingly, when the CLP potential was used only the orthorhombic form was found to be stable at these conditions; the monoclinic phase slowly distorted and became mechanically unstable. When the CMJJ potential was used, both the orthorhombic and monoclinic phases were found to be stable.

A comparison of the computed and experimental lattice parameters for the orthorhombic phase at 173 K is given in Table I, while Table II shows the same comparison for the monoclinic phase. Note that, regardless of the potential model, agreement between simulation and experiment is generally good, with no lattice parameter deviating from experiment by more than a few percent.

Experimental evidence suggests[38–42] that the conversion between the orthorhombic and monoclinic forms of the crystal is due to trans-gauche conformational changes in the alkyl group attached to the 1-position of the imidazolium ring. Specifically, the monoclinic form has a trans conformation for the dihedral angle between the first and second carbon atoms from the nitrogen atom of the ring, while this angle is in the gauche conformation in the orthorhombic form. The CLP and CMJJ force fields differ in how this dihedral angle is modeled and this may be the reason they yield different stabilities for the monoclinic form.

NPT simulations were then conducted on the liquid and orthorhombic crystal phases at eleven uniformly spaced temperatures between 300 and 400 K using the CLP and CMJJ potentials. Monoclinic simulations were also conducted using the CMJJ potential. Each simulation was carried out for a total of 1 ns, with enthalpies recorded over the final 0.75 ns. As an example of why direct MD simulations are ineffective at estimating melting points, Fig. 2 shows how the density of the orthorhombic crystal varies with temperature using the CLP potential. Although the experimental melting point of this crystal is about 339 K, a first order phase transition was

TABLE II. Comparison of experimental and simulation cell parameters at 173 K and 1 atm for the monoclinic phase of [C$_4$mim][Cl]. For this crystalline phase, only the CMJJ potential gave a stable crystal. Cell lengths a, b, and c are in Å and cell angles α, β, and γ are in degrees. Subscripted values depict statistical uncertainty in the final digit.

	a	b	c	α	β	γ
Experimental[a]	9.943	11.481	9.658	90.0	118.740	90.0
Simulation[b]	10.399$_8$	11.55$_1$	9.49$_1$	90.00$_5$	120.46$_6$	90.00$_6$

[a]Values obtained from Ref. 38.
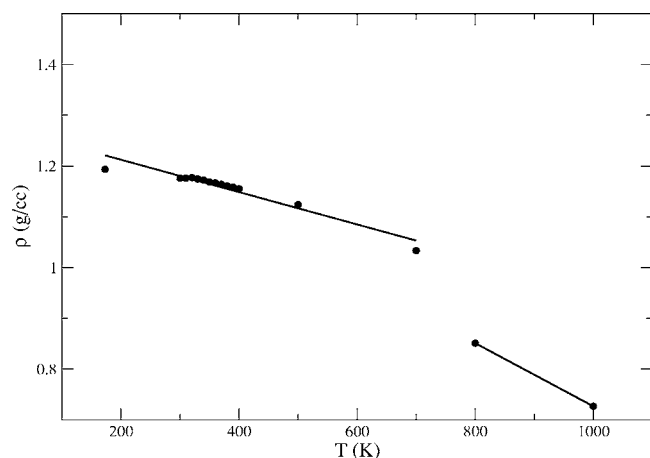[b]Values obtained from present study.

FIG. 2. Calculated crystal densities as a function of temperature for the orthorhombic form of $[C_4mim][Cl]$ using the CLP potential. Notice that very large superheating is required before an observed phase transition occurs.

not observed until a temperature above 700 K. This is consistent with the previously mentioned observation that extensive superheating is required to melt crystals in direct MD simulations, due to the large homogeneous nucleation free energy barriers. A qualitatively similar result was obtained with the CMJJ potential, although the phase transition was observed at about 500 K. As discussed later, this is most likely due to differences in how the dihedral angle potentials were parameterized.

Figure 3 is an example of how $-H/RT^2$ varies with temperature for the orthorhombic and liquid phases using the CLP potential. Similar results were obtained for the other systems. The results of these calculations were fit to a cubic spline and integrated according to Eq. (1) to obtain relative free energies. The reference temperature was arbitrarily taken as 300 K. An example of the resulting relative Gibbs free energy curves between the liquid and orthorhombic crystal for the CLP potential is shown in Fig. 4. Note that the curves are almost parallel, which means that the computed melting temperature is very sensitive to the free energy difference between the solid and liquid.

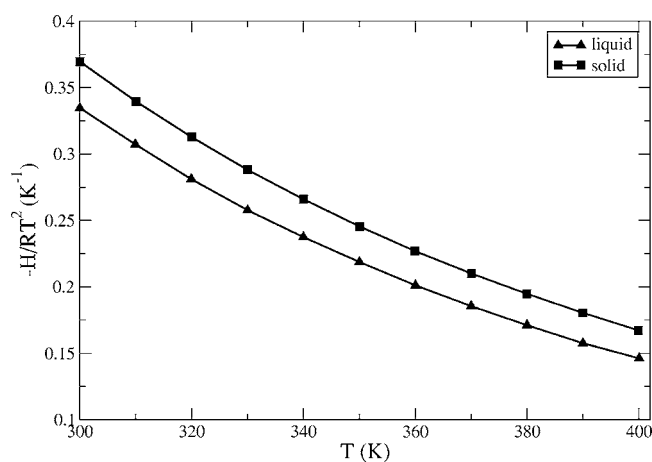Having obtained the relative free energy curves for each

FIG. 3. Plot of $-H/RT^2$ against T for the orthorhombic crystal and the liquid phase using the CLP potential.
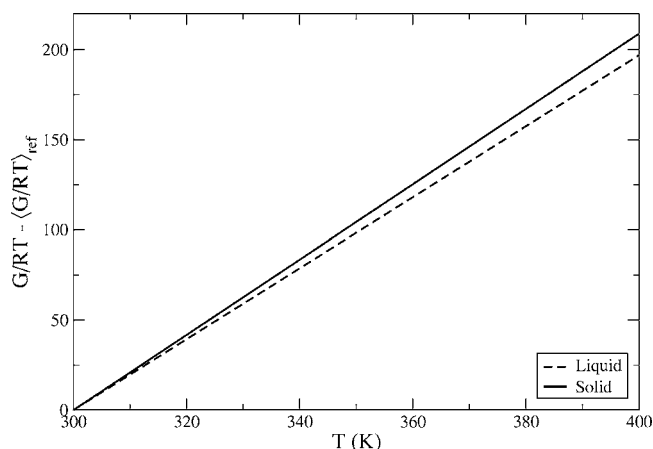

FIG. 4. Plot of $G/RT - \langle G/RT \rangle_{ref}$ against T for the orthorhombic crystal and liquid phase using the CLP potential. Similar results are obtained for the CMJJ potential.

system, the free energy difference between the liquid and crystal phases was determined by carrying out the thermodynamic integration cycle at 380 K. The choice of this temperature is arbitrary, as long as it is within the range in which relative Gibbs free energies have been calculated and not too far from the anticipated melting point. The first step in this process requires that crystal and liquid simulation boxes be generated at the appropriate density. Thus a flexible cell NPT simulation of a $3 \times 3 \times 3$ orthorhombic crystalline supercell was carried out at 1 atm pressure and 380 K. The resulting average supercell parameters were $a=28.82$ Å, $b=36.08$ Å, $c=25.95$ Å, $\alpha=90.05°$, $\beta=89.99°$, and $\gamma=90.03°$ for the CLP potential and $a=29.98$ Å, $b=35.68$ Å, $c=26.97$ Å, $\alpha=89.94°$, $\beta=90.06°$, and $\gamma=90.01°$ for the CMJJ potential. These results correspond to crystalline densities of 1.16 g/cm³ and 1.09 g/cm³, respectively. The unit cell angles were idealized to 90°, which had a negligible effect on the lattice energy. For the monoclinic solid phase using the CMJJ potential, the $3 \times 3 \times 4$ supercell dimensions were $a=32.32$ Å, $b=36.09$ Å, $c=39.53$ Å, $\alpha=90.00°$, $\beta=122.00°$, and $\gamma=90.00°$ and the density was found to be 1.07 g/cm³. These supercell boxes were then used for the calculations involving states (3)–(5). To obtain the boxes involved in states (1) and (2), liquid phase NPT simulations were carried out using cubic boxes at 1 atm and 380 K. Once liquid densities were determined for each potential model, liquid simulation boxes having the same shape as the respective crystalline boxes were constructed. The use of a box having the same shape as the crystalline box facilitates the transformation between states (2) and (3). The resulting CLP liquid phase simulation box had edge lengths of 30.03, 37.58, and 27.03 Å, resulting in a liquid density of 1.03 g/cm³. For the CMJJ potential, the dimensions of the liquid phase boxes used for conducting the thermodynamic integration cycle on orthorhombic and monoclinic crystal phases were 31.48, 37.46, 28.32 Å and 33.55, 37.46, 41.03 Å with $\beta=122°$, respectively. The CMJJ liquid density was 0.95 g/cm³.

The tethering potentials used in Eqs. (5) and (6) consist of a three-dimensional harmonic center of mass potential for the cation and anion, as well as additional weak harmonic

TABLE III. Baseline well strength parameters obtained from fitting a Gaussian to the vibrations about the centers of mass and subsequently scaling them down for both the CMJJ and CLP force fields.

Force field	Polymorph	κ/k_BT, Å^{-2}		
		COM	Cations	Anions
CLP	Orthorhombic	11.24	5.62	2.98
CMJJ	Orthorhombic	8.49	4.25	2.71
	Monoclinic	7.67	3.84	2.79

potentials for the heavy atoms of the cation. The hydrogen atoms of the cation were not tethered. The parameters for these tethering potentials were obtained in the following manner. Probability distributions for each atom and the center of mass of each ion about its average lattice position were collected during a NVT simulation of the solid and fit to Eq. (4). A complete listing of all center-of-mass and heavy atom tethering force constants is given in Table III. The well width parameters were fixed at $b_{ij}=0.9$ Å^{-2}, with the well-depth parameters given by $a_{ij}=\kappa/b$ for all i and j.

In our previous work,[35] it was recommended that the actual harmonic force constant used should be some fraction of the value computed from the NVT simulations, since the additional atom-specific potentials will help induce ordering, as will the weak nearest neighbor interactions. Therefore, a "base line" value of κ/k_BT was chosen to be 70% of the computed value for the center of mass of the cation and 35% of the computed value for the anion and the heavy atoms. For example, the base line center of mass tethering potentials for the CLP orthorhombic cation and anion is 11.24 and 2.98 Å^{-2}, respectively. As shown later, the use of overly strong tethering potentials can lead to weak first order phase transitions when moving between states (3) and (4) as well as between states (4) and (5). Therefore, several weaker tethering potential strengths were also investigated. We will refer to the base line case as the "100% well potential" case. Weaker tethering potentials that were 50%, 25%, and 10% of the base line values were also examined and will be called the "50%," "25%," and "10%" cases, respectively.

B. Thermodynamic cycle calculations for [C$_4$mim][Cl]

The results of the calculations along the first two steps of the thermodynamic integration cycle are shown in Figs. 5(a) and 5(b) for the orthorhombic CLP simulations. The curves are smooth and integration of the free energy presents no problem. The uncertainty in each $\langle \partial U/\partial \lambda \rangle_\lambda$ point is very small, while the uncertainties in the pressure are somewhat larger. Each point along the curve was obtained from an independent 2 ns simulation, with data collected the final 1.7 ns. The lines are Hermite polynomial fits to the data, which were integrated to obtain the free energy changes. Similar results were obtained for both polymorphs using the CMJJ potential.

Integration to states (4) and (5) presents more difficulties for the [C$_4$mim][Cl] system. Figures 6(a)–6(d) show the effect of decreasing the strength of the tethering potentials
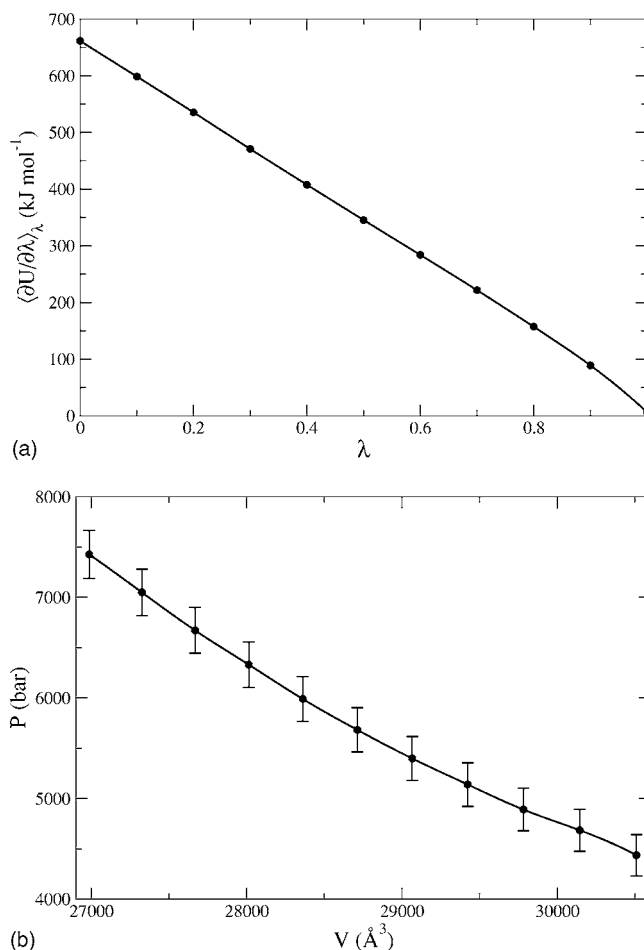

FIG. 5. Results of the thermodynamic integrations from a liquid to a weak fluid (a) and for the weak fluid between the liquid and crystalline densities (b). Lines are a guide for the eye. Results are for the orthorhombic CLP case.

from 100% of the base line value (a), to 50% of the base line value (b), to 25% of the base line value (c), and to 10% of the base line value (d) for the transformation between states (3) and (4). Note that the results shown here are for the CLP potential and the orthorhombic crystal, but similar results are observed for other systems. A first order phase transition is clearly evident for the first three cases, but not for the fourth (weakest tethering) case. For the strongest tethering (100%), the transition occurs early in the transformation, at roughly $\lambda=0.2$. For the weaker couplings, the transition occurs further to the right, at about $\lambda=0.38$ for the 50% case and at about $\lambda=0.73$ for the 25% case. In the region of the phase transition, convergence of the individual $\langle \partial U/\partial \lambda \rangle_\lambda$ values was unreliable due to strong fluctuations; the open symbols show approximate values for these cases, while filled symbols show results where convergence was possible. It is interesting that the transition occurs at roughly the same total coupling strength. In the 100% case, the transition occurs at a total coupling to the cation center of mass of approximately $\lambda(\kappa/k_BT)=0.2\times11.2$ Å$^{-2}=2.2$ Å^{-2}, while for the 50% case the transition occurs at $\lambda=0.38$ or $\lambda(\kappa/k_BT)=0.38\times5.6$ Å$^{-2}=2.1$ Å^{-2}. Similarly, for the 25% case, the transition occurs at $\lambda=0.73$, or $\lambda(\kappa/k_BT)=0.73\times2.8$ Å$^{-2}=2.04$ Å^{-2}. Using a coupling strength of just 10% of the
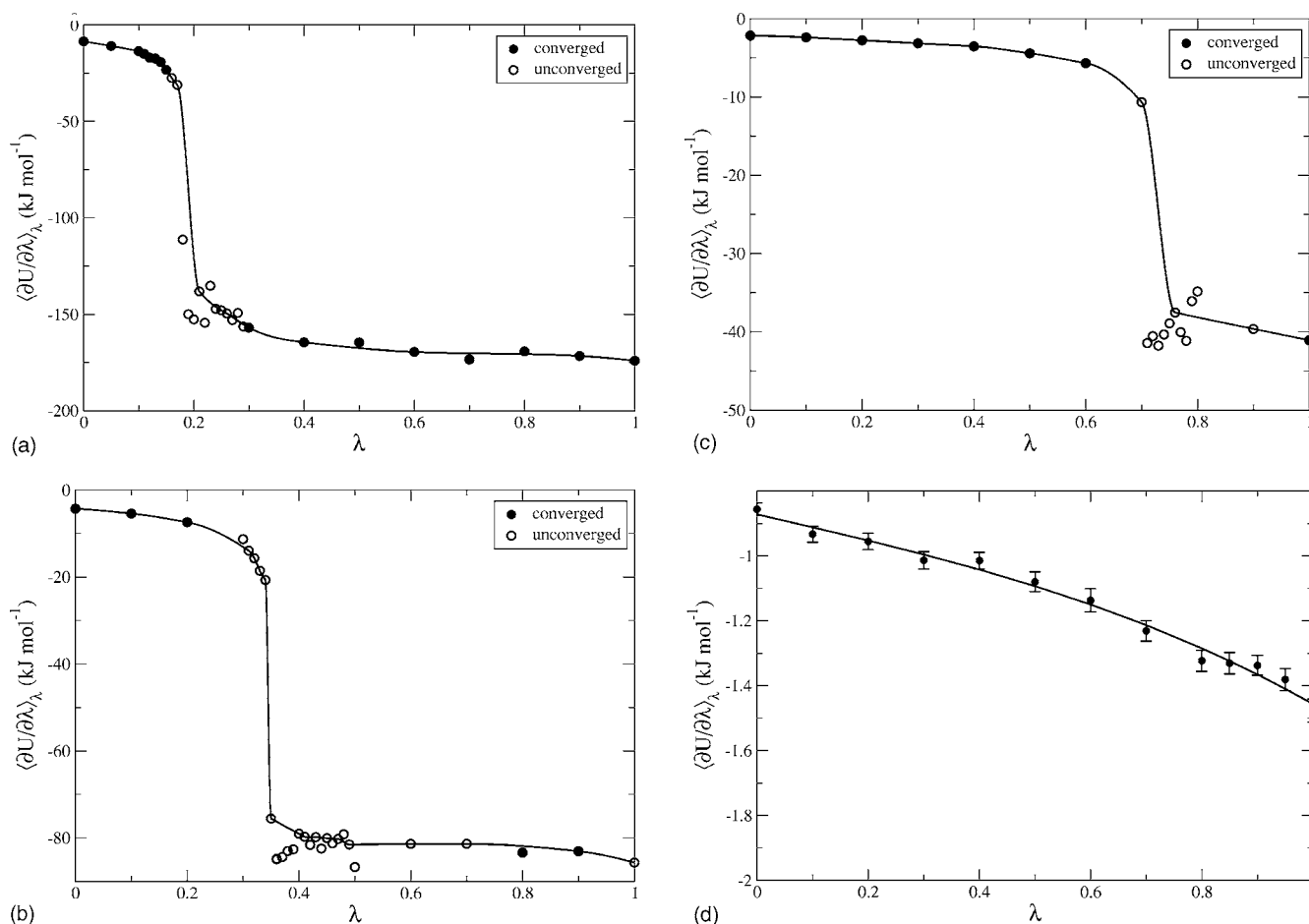
FIG. 6. Effect of tethering strength on the thermodynamic integration result from a weak fluid to an ordered weak state. Note the appearance of a phase transition for the three strongest tethering potentials. Open symbols are for unconverged simulations, while filled symbols are for converged simulations. Lines are a guide for the eye. All calculations were obtained using the CLP potential. (a) $(3)\rightarrow(4)$, 100% tether, (b) $(3)\rightarrow(4)$, 50% tether, (c) $(3)\rightarrow(4)$, 25% tether, and (d) $(3)\rightarrow(4)$, 10% tether.

base line causes the transition event to occur beyond the point at which $\lambda=1$. Assuming the transition would occur at $\lambda(\kappa/k_BT)=2.1$ Å^{-2} suggests that a transition would not occur until $\lambda\approx1.9$, well beyond the integration limit. Therefore, a smooth integration of the 10% case was possible. Notice also that as the coupling strength decreases, the magnitude of the free energy change along the path also decreases. The net result is that the appearance and location of phase transitions can be controlled by adjusting the tethering potentials, thereby enabling accurate thermodynamic integration along the transition path and avoiding first order phase transitions.

The strength of the tethering potentials also affects the integration from states (4) to (5), although no sharp transitions were observed along this path for any of the tethering potentials. Figure 7 shows the results of this simulation for the 10% case; the curve is smooth and a Hermite polynomial was fit to the data and integrated to estimate the free energy change for this transition.

The same procedure was used to obtain tethering potentials for the CMJJ potential. The tethering potential used for the cation centers of mass in the monoclinic crystal was 0.747 Å^{-2}, while for the anion centers of mass the value was found to be 0.279 Å^{-2}. For the orthorhombic phase the val-

ues were 0.849 and 0.271 Å^{-2}, respectively. No discontinuities or first order phase transitions were observed along the thermodynamic cycle in either case. Hence, it appears that the use of very weak tethering potentials for the order inducing step is a robust means of obtaining smooth integrable free energy change curves.
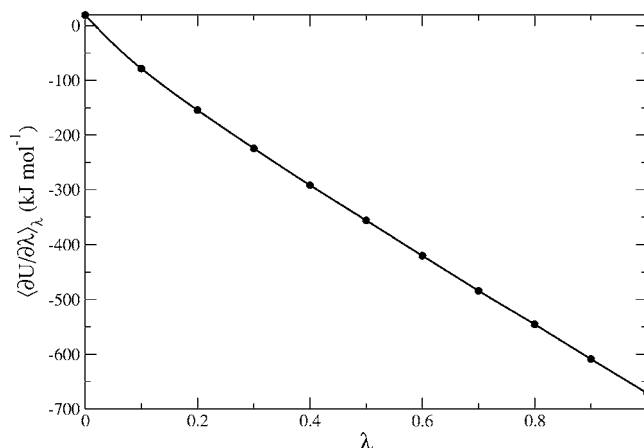

FIG. 7. Thermodynamic integration from weak tethered fluid (4) to untethered, fully interacting solid (5). The tethering potential was 10% of the base line case. The line is a guide for the eye.
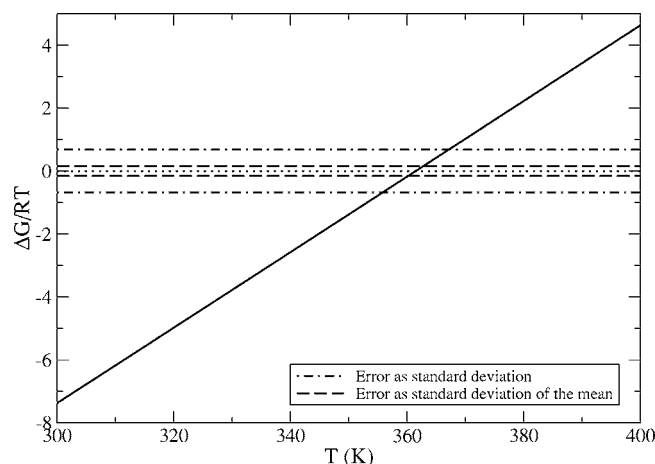
FIG. 8. The computed solid-liquid free energy difference as a function of temperature for the orthorhombic form of $[C_4mim][Cl]$ at 1 atm using the CLP potential. The dashed lines show the upper and lower bounds computed by using the standard deviation of the mean [Eq. (9)]. The dot-dashed lines show a larger uncertainty range, which is obtained by estimating the uncertainty as the standard deviation of the sums.

1. Melting point, enthalpy of fusion and polymorph stability for $[C_4mim][Cl]$

By adding up the free energy changes along the thermodynamic cycle, the absolute free energy difference between the liquid and the crystal phases at 380 K and 1 atm was computed. This gives the integration constant in Eq. (1) and enables the coexistence temperature to be determined. This is easiest to do by plotting $\Delta G/RT$ versus T and locating where the curve crosses zero. This has been done and the result is shown in Fig. 8 for the orthorhombic crystal using the CLP potential. Similar results were obtained for the CMJJ potential.

The enthalpies of fusion of the crystals were calculated by taking the difference between the average enthalpies of the crystalline and liquids phases. Table IV provides a comparison between the computed and experimental melting points and enthalpies of fusion for the two polymorphs. Note that if Eq. (9) is used, the estimated uncertainty in the melting point is roughly 1 °C. The actual uncertainty in the computed melting point is likely larger than what this analysis indicates, however, because the liquid and solid free energy curves are nearly parallel. This means that very small free energy differences between the solid and liquid phases result in large variations in the estimated melting point. The dot-dashed lines in Fig. 8 are uncertainties estimated from the standard deviations of the sums in Eq. (7) instead of the standard deviation of the mean. This uncertainty is likely a much more realistic estimate of the true uncertainty in the calculations and so was used when reporting melting points.

The results in Table IV show that both the CMJJ and

CLP potentials overestimate the melting point of the orthorhombic crystal by about 30 °C. The enthalpy of fusion of the orthorhombic crystal is captured quantitatively by the CMJJ potential, but the CLP potential overestimates the enthalpy by $7-10$ kJ/mol. Overall, however, both models do a reasonably good job capturing the solid-liquid equilibrium of this crystal polymorph, especially considering the sensitivity of the melting point to small differences in free energy. The major difference between the two models comes when analyzing the monoclinic polymorph. As mentioned before, it was not possible to obtain a mechanically stable monoclinic crystal with the CLP potential, even at 173 K, the temperature at which the experimental crystal structure was reported. It was thus not possible to compute a melting point or enthalpy of fusion for this model. The CMJJ potential did give a stable crystal phase, but the estimated melting temperature was on the order of $30-40$ °C higher than experiment, and the enthalpy of fusion was about 10 kJ/mol higher than what was observed experimentally. It thus appears that the CMJJ force field "overstabilizes" the monoclinic phase.

While there is consensus among the different experimental groups as to the melting point of the orthorhombic polymorph, there are significant discrepancies between the reported melting points of the monoclinic phase. Holbrey and co-workers[38] report a "plastic crystal transition" at 314 K, Nishikawa *et al.*[41] report a range of melting temperatures between 320 and 330 K, while Hamaguchi and Ozawa[42] report that melting points ranged from 320 to 340 K, depending on the crystal investigated. Nishikawa and co-workers suggest that this may be due to the presence of defects in the monoclinic phase, which would tend to reduce the observed melting point when compared to a defect-free crystal. This would explain why different melting points were obtained for different samples.

The relative stability of the different polymorphs is also not resolved. Holbrey and co-workers report that the orthorhombic phase is most stable, which is consistent with the overall trend in melting points. Hamaguchi and Ozawa,[42] on the other hand, observed that the orthorhombic polymorph spontaneously converted to the monoclinic form over a 24 h period at dry ice temperatures, suggesting that the monoclinic phase is the most thermodynamically stable at these temperatures. To investigate this, the free energy difference between the two polymorphs was computed as a function of temperature for the CMJJ potential. Figure 9 shows the result of this calculation. The CMJJ potential predicts that the monoclinic phase is indeed the thermodynamically stable phase at low temperature. The orthorhombic phase does not become the stable polymorph until about 390 K, which is above the melting point of both polymorphs. Thus, the calculations suggest that the orthorhombic phase is metastable

TABLE IV. Comparison of computed and experimental melting points and enthalpies of fusion for the two polymorphs of $[C_4mim][Cl]$. Experimental melting points are taken from Refs. 38, 41, and 42, while enthalpy of fusion data are from Ref. 41.

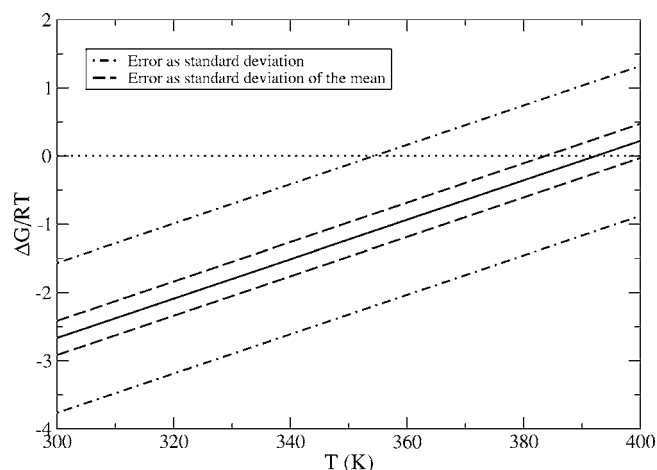| Polymorph	T_m^{expt} (K)	T_m^{CLP} (K)	T_m^{CMJJ} (K)	ΔH_{fus}^{expt} (kJ/mol)	ΔH_{fus}^{CLP} (kJ/mol)	ΔH_{fus}^{CMJJ} (kJ/mol)
Orthorhombic	337–339	365±6	369±7	18.5–21.5	28±3	19±4
Monoclinic	318–340	NA	373±4	9.3–14.5	NA	23±3

FIG. 9. The computed Gibbs free energy difference between the monoclinic and orthorhombic polymorphs of [C$_4$mim][Cl] using the CMJJ force field. The simulations predict that the monoclinic form is thermodynamically stable relative to the orthorhombic form at all temperatures below the melting point of either polymorph.

FIG. 10. (a) N$_1$-C$_7$-C$_8$-C$_9$ dihedral, (b) C$_7$-C$_8$-C$_9$-C$_{10}$ dihedral. Distribution of the dihedral angle between the first and second carbon (a) and between the second and third carbon (b) of the butyl chain of the cation in the liquid phase at 380 K for the CLP and CMJJ potentials. Notice that the CLP potential has a higher probability of having gauche conformations for the dihedral nearest the ring, while both potentials give nearly identical distributions for the other dihedral.

with respect to the monoclinic phase. It must be pointed out, however, that the differences in free energy between the two polymorphs are small and probably within the accuracy that can be expected of classical force field based calculations. It is interesting to note, however, that the lower entropy monoclinic polymorph containing all trans dihedral angles is predicted to be favored at low temperatures while the higher entropy gauche-trans orthorhombic phase becomes more stable as temperature increases. This may explain why Hamaguchi and co-workers observed the transition from orthorhombic to monoclinic at dry ice temperatures. Such transitions would most certainly be kinetically limited, however, which may explain why other groups have not observed this transition.

Due to the importance of the alkyl group dihedral angle distributions on crystal stability, an analysis was performed on the distribution of dihedral angles in the liquid phase. It has been observed through Raman spectroscopy[42] that the two cation alkyl chain rotational isomers present in the crystalline phase are also present in the liquid phase. It has been postulated that the presence of these two isomers hinders crystallization, thus lowering the melting point. The liquid phase simulations confirm the presence of these isomers. Figures 10(a) and 10(b) show the computed probability distributions for the dihedral angles between the first and second (defined as C$_7$ and C$_8$) and second and third (C$_8$ and C$_9$) carbon atoms from the imidazolium ring, respectively. By integrating the area beneath the different peaks, an estimate of the relative probability of each rotational isomer was obtained.

For the CLP force field, it was found that the gauche-trans (or GT) configuration occurred 47% of the time at 380 K. The next most probable conformation was trans-trans (TT), which occurred 26% of the time. Finally, the gauche-gauche (GG) and trans-gauche (TG) configurations were present 17% and 10% of the time, respectively. This suggests that in order to crystallize into the orthorhombic phase, the alkyl chains on over half of the cations must exhibit a con-
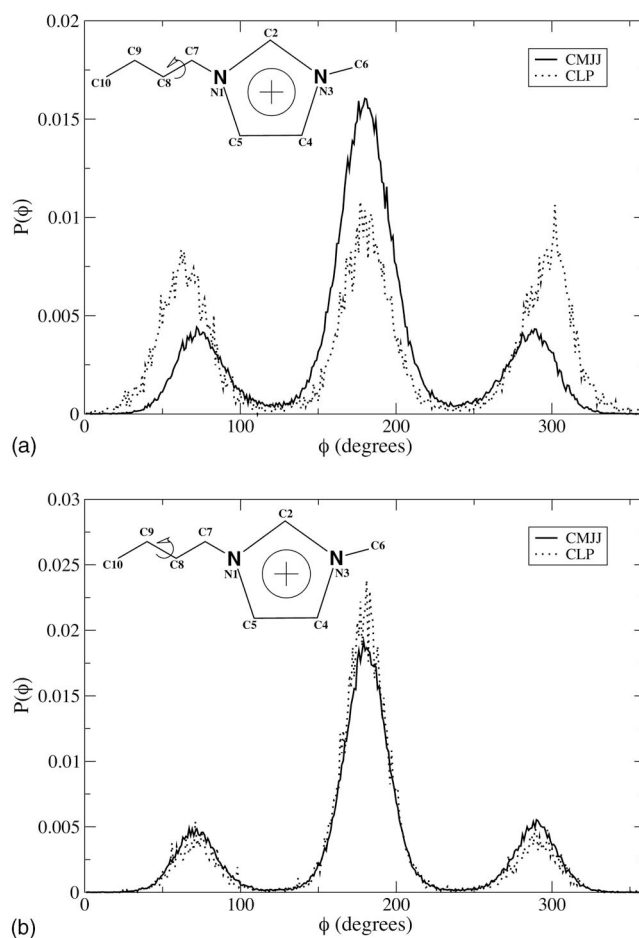
formational change to the GT state. Thus, the calculations are consistent with the postulate that the melting point of this ionic liquid is low due to the conformational degrees of freedom of the alkyl chain. For the CMJJ force field, the GT configuration occurs 22% and TT configuration occurs 43%. The TG and GG configurations occurred 23% and 12%, respectively. These results provide a likely explanation as to why the CMJJ potential predicts the monoclinic phase to be the more stable one. It "favors" TT configurations in the liquid phase and thus fewer molecules need to undergo dihedral rearrangement to convert to the monoclinic phase. Conversely, the CLP force field favors GT configurations, thus stabilizing the orthorhombic phase to a greater extent. Figure 11 shows a plot of total dihedral energy for the dihedral angle about the C$_7$-C$_8$ bond. The plot shows that the CMJJ force field is trifold symmetric in 360°. This means that the energy barriers to go from the trans configuration to the gauche configuration and vice versa are the same. This implies that the CMJJ potential should predict similar melting points and free energies for both the polymorphs, which is confirmed by the calculations. On the other hand, the CLP force field has a high energy barrier to go from the gauche
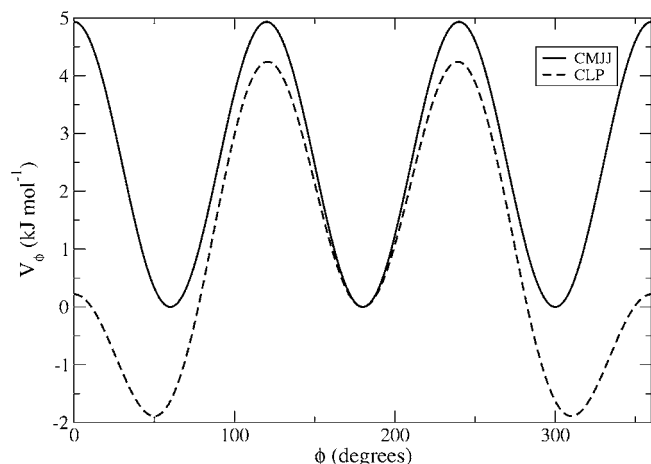
FIG. 11. Comparison of the CLP and CMJJ dihedral potential energy profiles for the dihedral angles with C_7 and C_8 as the central atoms. This energy does not include 1–4 Lennard–Jones interactions.

TABLE V. Comparison of melting points across different well strengths against experiment for $[C_4mim][Cl]$.

Well strength (%)	T_m^{sim} (K)	$T_m^{expt\ a}$ (K)
		339
100	355 ± 6	
50	348 ± 6	
25	359 ± 6	
10	365 ± 6	

[a]From Ref. 38.

configuration to the trans configuration. This means that once a molecule gets into a gauche energy "well," it will remain there for a long time. This appears to stabilize the orthorhombic crystal to a greater extent than what is observed with the CMJJ potential. This explains why direct simulations of the orthorhombic crystal does not lead to homogeneous nucleation until 700 K for the CLP potential (see Fig. 2) but the CMJJ crystal nucleates at 500 K. Moreover, the large dihedral energy barrier in the CLP potential likely inhibits the stability of the monoclinic phase. These findings are puzzling, because the CLP potential was developed by carefully parameterizing the alkyl chain dihedral potential against high-level quantum calculations, while the CMJJ dihedral potential parameters were adopted from similar compounds in the CHARMM force field.[51] It is possible that more accurate models could be developed by conducting parameterizations in the condensed phase rather than on isolated gas phase ions. This issue certainly requires more attention.

IV. ANALYSIS OF THE EFFECT TETHERING POTENTIALS HAVE ON COMPUTED MELTING POINTS

The calculations outlined earlier point out the importance of the adjusting the tethering potentials to avoid first order phase transitions in the thermodynamic path between the weak fluid [state (3)] and ordered weak fluid [state (4)]. Although the systems with the 100%, 50%, and 25% tethering potentials exhibited first order phase transitions between states (3) and (4), it is interesting to see how much this affects the estimated melting point. In other words, is it possible to "integrate through" the phase transition and still get a reasonable estimate of the melting point? To examine this question, Hermite polynomials were fit to the curves in Figs. 6(a)–6(c), assuming the unconverged points were valid. Integrations were also performed from the weak tethered system to the solid for these three cases; these curves did not show a phase transition regardless of the tethering potential. Table V shows the results of the calculations, along with the estimated error for the orthorhombic CLP case. It is remarkable that, despite the presence of a clear first order phase

transition in the strongly tethered systems, the estimated melting point is nearly the same in all cases. In fact, the three strongly tethered cases agree slightly better with the experimental melting point than does the weakly tethered system, although this is probably fortuitous. The apparent insensitivity of the melting point to the accuracy of the integration from weak fluid to a tethered weak system can be understood by looking at the relative magnitude of the free energy changes along each step of the thermodynamic cycle, as shown in Table VI. There is a significant amount of cancellation among the different steps of the cycle, such that the sum of ΔA_{34} and ΔA_{45} is roughly constant regardless of the tethering potential. This is encouraging, though it is not clear that all systems will exhibit this type of behavior.

The fact that nearly the same melting point is found for $[C_4mim][Cl]$ despite vastly different tethering potentials suggests that the method introduced here is relatively insensitive to the choice of these empirical tethering potentials and thus is a robust method for determining melting points. Since the present study is the first time the melting point of $[C_4mim]$ $\times[Cl]$ has been investigated by simulation, however, it is not possible to validate this claim against other accepted simulations. To do this, model systems must be examined for which there is consensus on the melting point. The pseudosupercritical path sampling approach used in the present study has been validated on the Lennard–Jones system[34] for which the melting point is known. However, no parametric analysis has been performed on this test system to see how the computed melting point might change with different tethering parameters.

To perform this analysis, 864 Lennard–Jones atoms were simulated in the liquid and solid phase. A $3 \times 3 \times 3$ face-centered-cubic (fcc) unit cell was simulated for the solid. Relative Gibbs free energy curves were generated using NPT MD simulations at $P^* = 1.0$ and regular temperature intervals between $T^* = 0.5$ and $T^* = 0.95$. For argon, this would correspond to a pressure of 417 bar and a temperature range of 60–114 K. The Nosé–Hoover thermostat-barostat algorithm[46] was used, allowing isotropic cell fluctuations. For the thermodynamic cycle calculations, NVT MD simulations were performed using the Nosé–Hoover thermostat at a temperature of $T^* = 0.7$. The simulations were carried out for 400 ps using a time step of 4 fs. This time was found to be adequate to achieve equilibration and collect statistically meaningful data. The potential was cutoff at 2.8σ and standard long range corrections were applied.

As with $[C_4mim][Cl]$, the strength of the tethering potential was estimated by carrying out NVT MD simulations

TABLE VI. Individual contributions to [C$_4$mim][Cl] solid-liquid free energy difference at 380 K and 1 atm. Note that the PV term is negligible, such that $\Delta A \approx \Delta G$. All energies are in kJ/mol. Subscripted values depict statistical uncertainty in the final digit.

Well strength (%)	ΔA_{12}	ΔA_{23}	ΔA_{34}	ΔA_{45}	ΔG
100	344.7$_2$	11.3$_4$	−137.9$_1$	−208.8$_2$	9.2$_5$
50	344.7$_2$	11.3$_4$	−53.4$_1$	−290.5$_1$	12.0$_5$
25	344.7$_2$	11.3$_4$	−14.06$_4$	−334.0$_2$	7.9$_5$
10	344.7$_2$	11.3$_4$	−1.12$_1$	−349.3$_2$	5.6$_5$

of the fcc crystal and computing the fluctuations of each atomic position about its mean position. The fluctuations were fit to Eq. (4) and found to yield a force constant of $\kappa/k_B = 680$ K/Å^2. Taking 35% of this as a base line tethering potential yields a value of $\kappa/k_B = 238$ K/Å^2. To examine how the tethering potential affects the integration path from weak fluid to a weakly interacting ordered system, harmonic tethering force constants of κ/k_b of 100, 400, and 2000 K/Å^2 were also used.

As can be seen in Fig. 12, a weak coupling gives a smooth curve with no indication of a first order phase transition. However, as the tethering potential increases in strength, evidence of a weak transition appears. As with the ionic liquid, the transition shifts to smaller values of λ as the tethering potential increases in strength. It is also observed in

Fig. 13 that a discontinuity appears at very high tethering potentials during the integration from the tethered system [state (4)] to the fully interacting crystal [state (5)].

Surprisingly, good estimates are obtained for the melting point of the Lennard–Jones system even if one integrates the curves having discontinuities. Table VII shows that the calculated melting point for each tethering potential is T^* = 0.74, and is insensitive to the tethering potential strength. The results are in good agreement with accepted values. This suggests that the present method is robust within a fairly broad range of tethering potentials and that results do not depend strongly on the choice of tethering parameters. It is advised, however, that tethering potentials be chosen to avoid phase transitions.
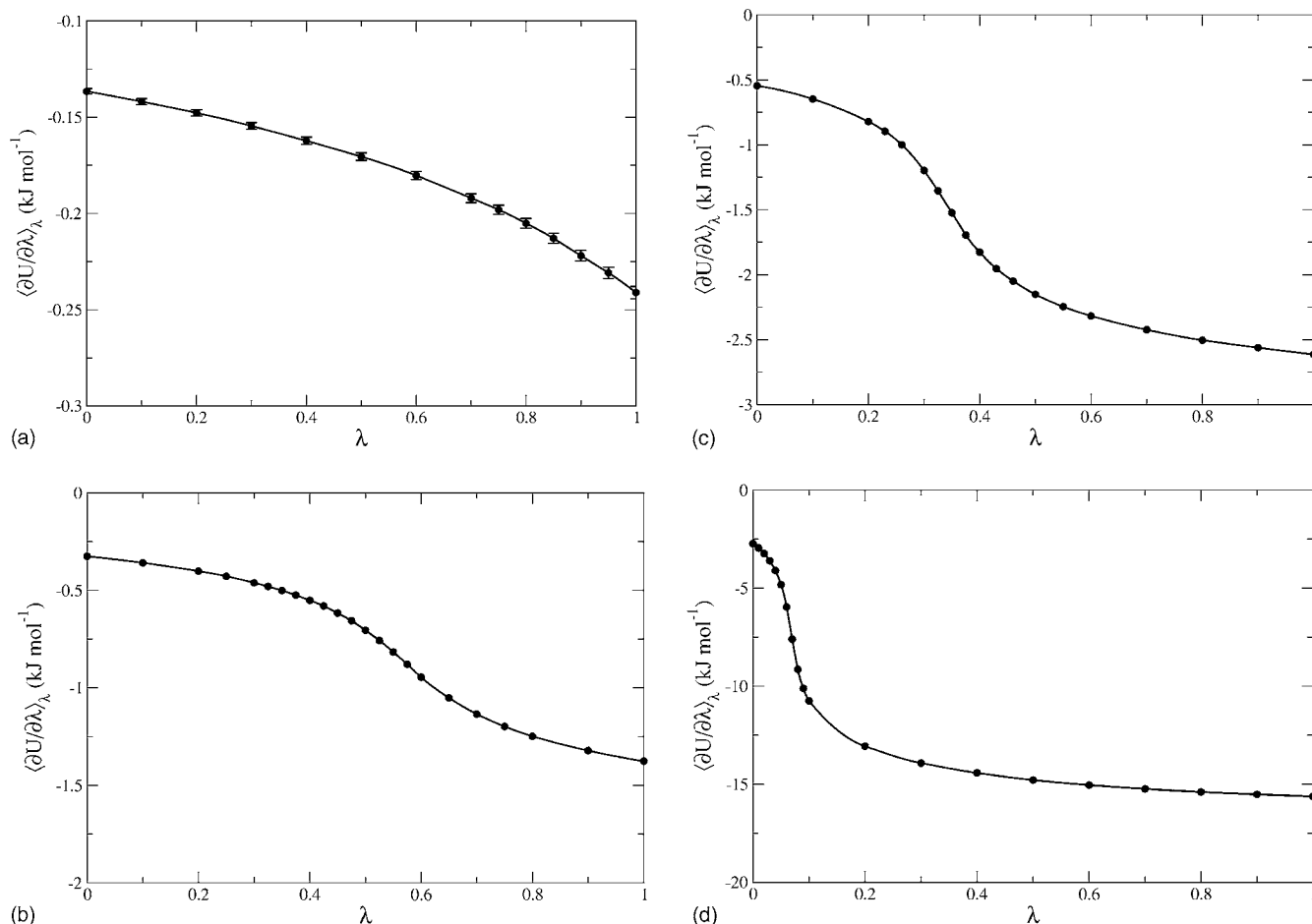

FIG. 12. The transition from weakly interacting fluid to weakly interacting ordered state for the Lennard–Jones fluid at various tethering potentials. Notice the appearance of a weak phase transition as the tethering potential increases in strength, although each simulation point converged to a stable average. Lines are a guide for the eye. (a) $\kappa/k_B = 100$ K/Å^2, (b) $\kappa/k_B = 238$ K/Å^2, (c) $\kappa/k_B = 400$ K/Å^2, and (d) $\kappa/k_B = 2000$ K/Å^2.
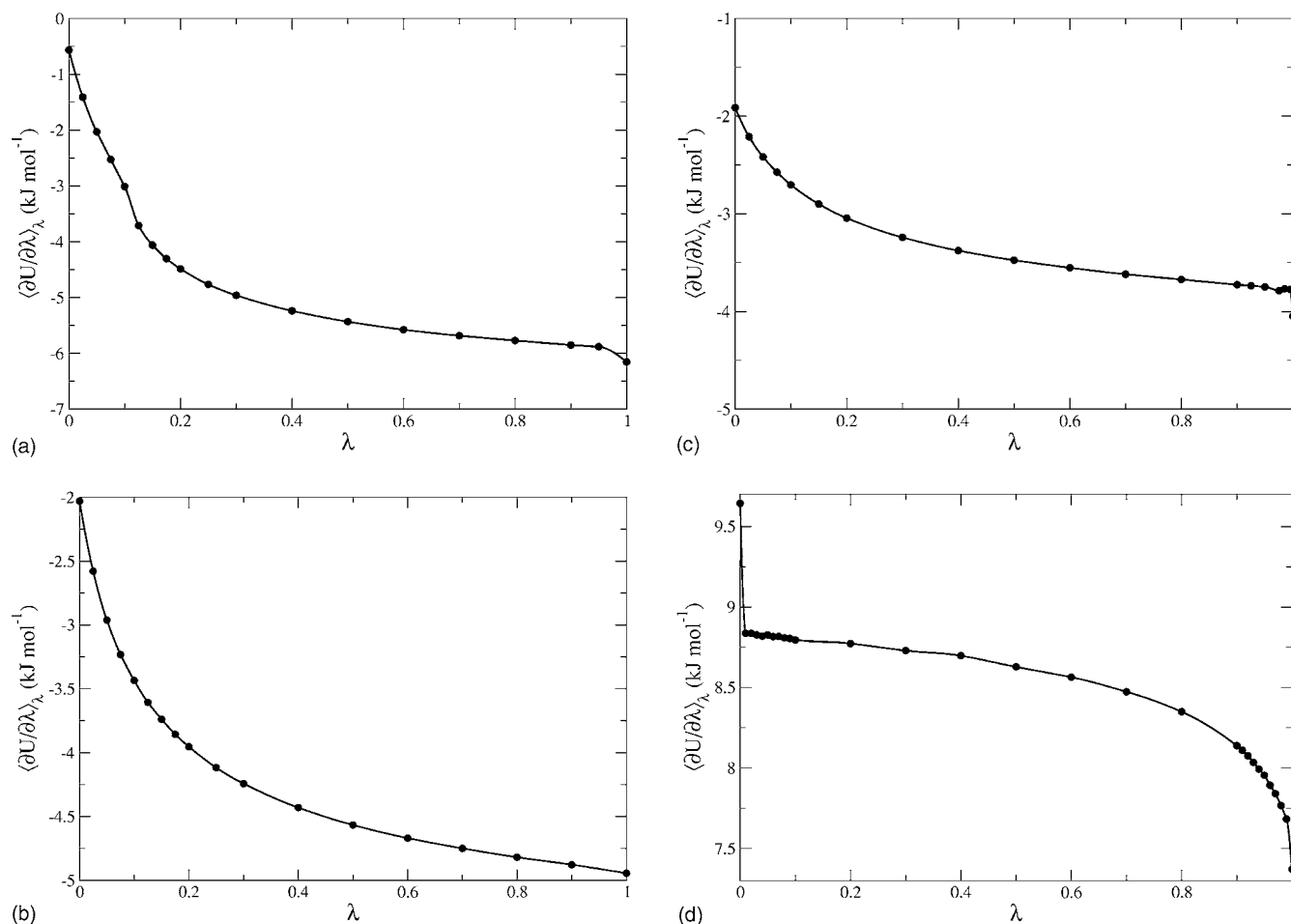
FIG. 13. The transition from weakly interacting ordered state to fcc crystal for the Lennard–Jones fluid as a function of tethering potential. Lines are a guide for the eye. (a) $\kappa/k_B=100$ K/Å^2, (b) $\kappa/k_B=238$ K/Å^2, (c) $\kappa/k_B=400$ K/Å^2, and (d) $\kappa/k_B=2000$ K/Å^2.

V. CONCLUSIONS

The melting point and thermodynamic stability of two polymorphs of 1-n-butyl-3-methylimidazolium chloride have been computed at atmospheric pressure using a rigorous free energy-based atomistic simulation method. The computed melting point of the orthorhombic phase is found to be between 365 and 369 K, depending on the force field used. This compares reasonably well with the experimental value, which ranges from 337 to 339 K. Enthalpies of fusion for the orthorhombic phase are computed to be 19 kJ/mol using the CMJJ force field, and 28 kJ/mol when the CLP force field is used. Again, these values are in good agreement with the accepted range of 18.5−21.5 kJ/mol.

TABLE VII. Comparison of melting points across different well strengths against experiment for LJ. Subscripted values depict statistical uncertainty in the final digit.

κ/k_B (K/Å^2)	$T_m^{*\mathrm{sim}}$	$T_m^{*\mathrm{EOS}}$ [a]
		0.77
100	0.74$_2$	
238	0.74$_2$	
400	0.74$_2$	
2000	0.74$_3$	

[a]Predicted by the equation of state (Ref. 52).

Only the CMJJ force field yielded a stable monoclinic phase; the monoclinic crystal was mechanically unstable when simulated with the CLP potential. The CMJJ force field yielded a melting point for this polymorph of 373 K, while various experimental measurements list the value between 318 and 340 K. The computed enthalpy of fusion was 23 kJ/mol, while the experimental value is reported to be 9.3−14.5 kJ/mol.

There is disagreement among experimental groups as to which polymorph is thermodynamically stable. Calculations using the CMJJ potential suggest that the monoclinic form is more thermodynamically stable than the orthorhombic form at low temperature. However, the free energy differences between the two polymorphs are on the order of the accuracy expected from classical force fields, so unambiguous determination of thermodynamic stability is probably not possible. Since the CLP potential did not yield a stable monoclinic phase, this model predicts that the orthorhombic phase is the only stable polymorph.

In agreement with Raman studies, the simulations show that the alkyl group contains both trans and gauche conformations in the liquid phase. The simulations find that just under 50% of the liquid phase alkyl group dihedral conformations are gauche-trans, while 26% are trans-trans for the CLP potential. For the CMJJ potential, it was found that

around 22% and 43% of the molecules in the liquid phase are in gauche-trans and trans-trans, respectively.

It was observed that, depending on the strength of the tethering potential used in organizing the fluid phase during the thermodynamic integration, a first order phase transition could appear. The appearance and location of this transition could be controlled by changing the strength of the tethering potential. By making the tethers sufficiently weak, the transition could be avoided, thereby enabling reliable integration. This phenomenon was also found to occur with the Lennard–Jones system. Surprisingly, it was found that the computed melting point is insensitive to whether such a transition occurs or not. That is, integrating "through" a phase transition yielded essentially the same melting point as did integrating over a smoothly varying transition path. This suggests that the pseudosupercritical path sampling approach used in this study is robust over a wide range or parameters, although it is recommended that parameters be adjusted to avoid strong variations along thermodynamic paths.

ACKNOWLEDGMENTS

[1] K. R. Seddon, Nat. Mater. **2**, 363 (2003).

[2] P. Walden, Bulletin de l'Academie Imperiale des Sciences de St. Petersbourg, 1914, pp. 405–422.

[3] S. Sugden and H. Wilkins, J. Chem. Soc. 1291 (1929).

[4] M. Freemantle, Chem. Eng. News **81**, 9 (2003).

[5] J. D. Holbrey and K. R. Seddon, Clean Prod. Process. **1**, 223 (1999).

[6] A. R. Katritzky, A. Lomaka, R. Petrukhin, R. Jain, M. Karelson, A. E. Visser, and R. D. Rogers, J. Chem. Inf. Comput. Sci. **42**, 71 (2002).

[7] A. R. Katritzky, R. Jain, A. Lomaka, R. Petrukhin, M. Karelson, A. E. Visser, and R. D. Rogers, J. Chem. Inf. Comput. Sci. **42**, 225 (2002).

[8] D. M. Eike, J. F. Brennecke, and E. J. Maginn, Green Chem. **5**, 323 (2003).

[9] N. Sun, X. He, K. Dong, X. Zhang, X. Lu, H. He, and S. Zhang, Fluid Phase Equilib. **246**, 137 (2006).

[10] S. Trohalaki, R. Pachter, G. W. Drake, and T. Hawkins, Energy Fuels **19**, 279 (2005).

[11] M. P. Allen and D. J. Tildesley, *Computer Simulation of Liquids* (Clarendon, Oxford, 1987).

[12] C. G. Hanke, S. L. Price, and R. M. Lynden-Bell, Mol. Phys. **99**, 801 (2001).

[13] T. I. Morrow and E. J. Maginn, J. Phys. Chem. B **106**, 12807 (2002).

[14] C. J. Margulis, H. A. Stern, and B. J. Berne, J. Phys. Chem. B **106**, 12017 (2002).

[15] J. de Andrade, E. S. Boes, and H. Stassen, J. Phys. Chem. B **106**, 3546 (2002).

[16] J. N. Canongia Lopes, J. Deschamps, and A. A. H. Pádua, J. Phys. Chem. B **108**, 2038 (2004).

[17] M. G. Del Pópolo and G. A. Voth, J. Phys. Chem. B **108**, 1744 (2004).

[18] X. P. Wu, Z. P. Liu, S. P. Huang, and W. C. Wang, Phys. Chem. Chem. Phys. **7**, 2771 (2005).

[19] J. N. Canongia Lopes, J. Deschamps, and A. A. H. Pádua, J. Phys. Chem. B **108**, 2038 (2004).

[20] S. Alavi and D. L. Thompson, J. Phys. Chem. B **109**, 18127 (2005).

[21] C. Cadena and E. J. Maginn, J. Phys. Chem. B **110**, 18026 (2006).

[22] S. Alavi and D. L. Thompson, J. Chem. Phys. **122**, 154704 (2005).

[23] A. B. Belonoshko, R. Ahuja, and B. Johansson, Phys. Rev. B **61**, 11928 (2000).

[24] P. M. Agrawal, B. M. Rice, and D. L. Thompson, J. Chem. Phys. **119**, 9617 (2003).

[25] P. M. Agrawal, B. M. Rice, and D. L. Thompson, J. Chem. Phys. **118**, 9680 (2003).

[26] G. F. Velardez, S. Alavi, and D. L. Thompson, J. Chem. Phys. **119**, 6698 (2003).

[27] J. R. Morris, C. Z. Wang, K. M. Ho, and C. T. Chan, Phys. Rev. B **49**, 3109 (1994).

[28] A. B. Belonoshko and L. S. Dubrovinsky, Am. Mineral. **81**, 303 (1996).

[29] H. L. Tepper and W. J. Briels, J. Chem. Phys. **115**, 9434 (2001).

[30] B. B. Laird and R. L. Davidchack, J. Phys. Chem. B **109**, 17802 (2005).

[31] J. Anwar, D. Frenkel, and M. G. Noro, J. Chem. Phys. **118**, 728 (2003).

[32] D. Frenkel and A. J. C. Ladd, J. Chem. Phys. **81**, 3188 (1984).

[33] N. B. Wilding and A. D. Bruce, Phys. Rev. Lett. **85**, 5138 (2000).

[34] D. M. Eike, J. F. Brennecke, and E. J. Maginn, J. Chem. Phys. **122**, 014115 (2005).

[35] D. M. Eike and E. J. Maginn, J. Chem. Phys. **124**, 164503 (2006).

[36] G. Grochola, J. Chem. Phys. **120**, 2122 (2004).

[37] G. Grochola, J. Chem. Phys. **122**, 046101 (2005).

[38] J. D. Holbrey, W. M. Reichert, M. Nieuwenhuyzen, S. Johnston, K. R. Seddon, and R. D. Rogers, Chem. Commun. **2003**, 1636.

[39] S. Saha, S. Hayashi, A. Kobayashi, and H. Hamaguchi, Chem. Lett. (Jpn.) **32**, 740 (2003).

[40] S. Hayashi, R. Ozawa, and H. Hamaguchi, Chem. Lett. (Jpn.) **32**, 498 (2003).

[41] K. Nishikawa, S. Wang, H. Katayanagi, S. Hayashi, H. Hamaguchi, Y. Koga, and K. Tozaki, J. Phys. Chem. B **111**, 4894 (2007).

[42] H. Hamaguchi and R. Ozawa, Adv. Chem. Phys. **131**, 85 (2005).

[43] See http://therm10.univ-bpclermont.fr/~apadua/research/il.ff, Agilio Padua has made available online the updated ionic liquid force field parameters from his various publications. This website was accessed on February 2007 to obtain updated parameters for the CLP force field.

[44] K. P. Jensen and W. L. Jorgensen, J. Chem. Theory Comput. **2**, 1499 (2006).

[45] S. Melchionna, G. Ciccotti, and B. L. Holian, Mol. Phys. **78**, 533 (1993).

[46] G. J. Martyna, M. E. Tuckerman, D. J. Tobias, and M. L. Klein, Mol. Phys. **87**, 1117 (1996).

[47] U. Essmann, L. Perera, M. L. Berkowitz, T. Darden, H. Lee, and L. G. Pedersen, J. Chem. Phys. **103**, 8577 (1995).

[48] W. Smith and T. R. Forester, J. Mol. Graph. **14**, 136 (1996).

[49] J. C. Phillips, R. Braun, W. Wang, J. Gumbart, E. Tajkhorshid, E. Villa, C. Chipot, R. D. Skeel, L. Kale, and K. Schulten, J. Comput. Chem. **26**, 1781 (2005).

[50] G. J. Martyna, D. J. Tobias, and M. L. Klein, J. Chem. Phys. **101**, 4177 (1994).

[51] A. D. Mackerell, J. Wiorkiewicz-Kuczera, and M. Karplus, J. Am. Chem. Soc. **117**, 11946 (1995).

[52] M. A. van der Hoef, J. Chem. Phys. **113**, 8142 (2000).